FUSION OF MAGNETIC RESONANCE AND ULTRASOUND IMAGES USING GUIDED FILTERING: APPLICATION TO ENDOMETRIOSIS SURGERY

Youssra El Bennioui[1], *Abderrahim Halimi*[2], *Adrian Basarab*[3], *Jean-Yves Tourneret*[1]

[1]Institut de Recherche en Informatique de Toulouse, CNRS UMR 5505, Univ Toulouse, France / TéSA Laboratory, Toulouse, France

[2]School of Engineering and Physical Sciences, Heriot-Watt University, Edinburgh, EH14 4AS, United Kingdom

[3] Université Claude Bernard Lyon 1, CNRS, Inserm, CREATIS UMR 5220, U1294, France

ABSTRACT

This paper studies a new fusion method designed for magnetic resonance (MR) and ultrasound (US) images, with a specific focus on endometriosis diagnosis. The proposed method is based on guided filtering, leveraging the advantages of this technique to enhance the quality of fused images. The fused image is a weighted average of base and detail images from the MR and US images. The weights assigned to the US image account for the presence of speckle noise, a common challenge in US imaging whereas the weights assigned to the MR image allow the contrast of the fused image to be enhanced. The effectiveness of the method is evaluated using synthetic and phantom data, showing promising results. The image provided by the proposed fusion method holds potential for enhancing visualization and aiding decision-making in endometriosis surgery, offering a valuable contribution to the field of medical image fusion.

Index Terms— Image fusion, MRI, ultrasound imaging, endometriosis, guided filtering, despeckling.

1. INTRODUCTION

Endometriosis is a debilitating medical disease characterized by the abnormal growth of endometrial tissue outside the uterus, causing significant pain and affecting more than ten percent of women worldwide. One prominent challenge is the prolonged diagnosis period, averaging seven years, during which the endometrial tissue can extensively spread and impact various pelvic organs. It is linked to severe pelvic pain, infertility risks, and an increased susceptibility to ovarian cancers. The primary treatment for endometriosis is the laparoscopy. The success of this surgery relies significantly on the accurate insights provided by preoperative medical imaging workup, such as the precise localization of the endometrial lesion and its depths of infiltration. Imaging modalities, mainly magnetic resonance (MR) and ultrasound (US), play a crucial and complementary role in precisely identifying and assessing the extent of endometriosis lesions, enabling surgeons to make informed decisions, avoid unnecessary radical procedures and enhance the efficiency of the intervention.

MR and US images have been used in many clinical diagnosis and guided surgery applications. They exploit different physical phenomena and thus have their own advantages and limitations. In particular, depending on the choice of the probe central frequency, US imaging offers well-resolved images and high frame rate compared to MRI. However, this comes at the expense of a notably low signal-to-noise ratio (SNR), reduced contrast, presence of speckle noise, and a restricted field of view. On the contrary, MR images provide a wide field of view of the patient anatomy with a good SNR ratio, a high contrast but a limited spatial resolution.

Previous observations greatly support the need for MR/US image fusion. Efficient fusion methods have been proposed for MR and single-photon emission computed tomography (SPECT) [1], MRI and computed tomography (CT) [2], or positron emission tomography (PET) and CT [3]. An innovative US-MR image fusion algorithm, combining two inverse problems for MR image super-resolution and US image despeckling was also proposed for endometriosis diagnosis [4] [5], yielding a fused image with comparable spatial resolution to US images, along with signal-to-noise ratio and contrast close to MR images.

Image fusion with guided filtering was also proposed to produce highly informative images through merging multiple images [6], [7]. It is based on a two-scale decomposition of an image into a base layer containing large scale variations in intensity, and a detail layer capturing small scale details. The guided filtering-based weighted average technique studied in [7] makes full use of spatial consistency for fusion of the base and detail layers.

This paper studies a new MR/US fusion method exploiting the principles of guided filtering. The proposed approach incorporates properties of the two imaging modalities. Specifically, Gaussian noise associated with MR images and speckle noise affecting US images are taken into account when determining the weights for fusion, ensuring the fused image is an enhanced informative image, which is very useful for endometriosis diagnosis. The proposed fusion method is evaluated on an experimental phantom and realistic data generated from an in vivo MRI volume. The remainder of the paper is organized as follows. Section 2 briefly reviews the principles of guided image filtering. The proposed fusion algorithm is introduced in Section 3. Experiments are presented and discussed in Section 4. Conclusions and perspectives are finally reported in Section 5.

2. IMAGE GUIDED FILTERING

Using the notations of [7], the guided filter involves a guidance image $I = (I_i)$, an input image $P = (P_i)$ and an output image $O = (O_i)$ that are vectorized, where i is the pixel index. This filter assumes that the output O is a linear transformation of the guidance image I in a local window ω_k, i.e.,

$$O_i = a_k I_i + b_k, \qquad \forall i \in \omega_k, \qquad (1)$$

where ω_k is a window of radius r centering the pixel k, and (a_k, b_k) are some coefficients assumed to be constant in ω_k, that can be estimated by minimizing the squared difference between the output image O and the input image P:

$$E(a_k, b_k) = \sum_{i \in \omega_k} \left[(a_k I_i + b_k - P_i)^2 + \epsilon a_k^2 \right], \qquad (2)$$

where ϵ is a regularization parameter that needs to be adjusted by the user. Straightforward computations detailed in [6] show that the coefficients a_k and b_k have the following closed-form expressions:

$$a_k = \frac{\frac{1}{|\omega_k|} \sum_{i \in \omega_k} I_i P_i - \mu_k \bar{P}_k}{\delta_k + \epsilon}, \qquad (3)$$
$$b_k = \bar{P}_k - a_k \mu_k,$$

where μ_k and δ_k are the mean and variance of the guidance image I in ω_k, $|\omega_k|$ is the number of pixels in ω_k, $\bar{P}_k$ is the mean of the input image P in ω_k, and ϵ represents the blur degree of the guided filter. Considering that pixel i is involved in all the overlapping windows ω_k that cover i, the value of O_i in (1) is not identical when it is computed in different windows. A simple strategy is to average all the possible values of O_i, which means that, after computing (a_k, b_k) for all windows ω_k in the image, the filtered output is:

$$O_i = \frac{1}{|\omega_k|} \sum_{k | i \in \omega_k} (a_k I_i + b_k). \qquad (4)$$

Finally, according to [6], (4) can be further converted as

$$O_i = \sum_j W_{i,j}(I_i) P_j, \qquad (5)$$

where $W_{i,j}$ is a function of the guidance image I, assumed independent of P. In this paper, the guided filter operation will be denoted as $\text{GF}_{r,\epsilon}(P, I)$.

3. IMAGE FUSION WITH A GUIDED FILTER

The image fusion model introduced in this section assumes that the MR and US images to be fused, denoted as I_{mri} and I_{us}, are already aligned, i.e., I_{mri} is a 2D image extracted from the MRI volume that best matches I_{us} and there is no geometric distortion between them, which can be obtained after

an appropriate pre-registration [8]. Inspired from prior work in image fusion using guided filtering [7], the proposed algorithm is based on MR and US image decompositions and subsequent weight computations. First, two-scale representations are obtained by applying an average filter to the MR and US images yielding base and detail images. Then, the base and detail MR and US images are weighted. A novel aspect is introduced by incorporating speckle-related considerations in the weight assignment for the US image.

3.1. Proposed fusion algorithm

Algo. 1 summarizes the different steps of the fusion model as detailed in the following sections: 1) Two-scale decomposition. 2) Weight construction for the MR image. 3) Weight construction for the US image. 4) MRI and US image fusion.

Algorithm 1 Fusion of MR and US images.

1: Input: I_{us}, I_{mri} and parameters r_1, ϵ_1, r_2, ϵ_2, patch size $|\omega|$, Z, K_1 and K_2
2: Two-scale decompositions of I_{us}, I_{mri} with (7)
3: Calculate $\bar{B}_{\text{mri}}$ and $\bar{D}_{\text{mri}}$ as explained in (9)
4: Calculate $\bar{B}_{\text{us}}$ and $\bar{D}_{\text{us}}$:
5:     a) Construct guidance images B_{us}^g and D_{us}^g using 3×3 averaging of B_{us} and D_{us}.
6:     b) Compute $W_{i,j}(B_{\text{us}}, B_{\text{us}}^g)$, $W_{i,j}(D_{\text{us}}, D_{\text{us}}^g)$ in (11)
7:     c) Compute $\bar{B}_{\text{us}}$ and $\bar{D}_{\text{us}}$ in (12)
8: Combine the base and detail layers for fusion

$$F = \bar{B}_{\text{mri}} + \bar{D}_{\text{mri}} + \bar{B}_{\text{us}} + \bar{D}_{\text{us}}. \qquad (6)$$

9: Output: Fused Image F

3.2. Two-scale decomposition

The base and detail layers of each image are obtained as:

$$\begin{aligned} B_{\text{mri}} &= I_{\text{mri}} * Z & ; & & B_{\text{us}} &= I_{\text{us}} * Z \\ D_{\text{mri}} &= I_{\text{mri}} - B_{\text{mri}} & ; & & D_{\text{us}} &= I_{\text{us}} - B_{\text{us}} \end{aligned} \qquad (7)$$

where Z is an average filter [9] and $*$ denotes 2D convolution. This two-scale decomposition is designed to partition each source image into a base layer capturing the significant variations in intensity at a larger scale, and a detail layer containing the finer details at a smaller scale.

3.3. Weight construction for the MR image

The weights for the MR image are constructed as in [7]. First, a Laplacian filter is applied to each source image to obtain the high-pass filtered images:

$$H_{\text{mri}} = I_{\text{mri}} * L, \; H_{\text{us}} = I_{\text{us}} * L,$$

where L is the 3×3 Laplacian filter. Then, the local average of the absolute value of these high-pass images is used to

construct the following saliency maps:

$$S_{\text{mri}} = |H_{\text{mri}}| * g_{r_g,\sigma_g}, \ S_{\text{us}} = |H_{\text{us}}| * g_{r_g,\sigma_g},$$

with g a Gaussian low-pass filter of size $(2r_g + 1) \times (2r_g + 1)$ and standard deviation σ_g. Subsequently, the weights are determined by constructing the following indicator:

$$P_{\text{mri}}^k = \begin{cases} 1 \text{ if } S_{\text{mri}}^k = \max\left(S_{\text{mri}}^k, S_{\text{us}}^k\right), \\ 0 \text{ otherwise}, \end{cases}$$

where S^k is the saliency value of the pixel k. The weight maps often exhibit noise that may produce artifacts to the fused image. This issue is usually addressed by incorporating spatial consistency, i.e., adjacent pixels with similar brightness or color should have comparable weights. This can be achieved by using guided filtering. Referring to (1) and (3), it becomes apparent that when the local variance at a position is very small, which means that the pixel is in a flat region in the guidance image, a_k tends to 0 and the filtering output tends to $\bar{P}_k$, i.e., the average of adjacent input pixels. In contrast, if the local variance at a pixel is significant, suggesting an edge region, a_k becomes very different from 0, so only the weights on one side of the edge are averaged. In both scenarios, pixels with similar brightness will have similar weights. Guided filtering is performed on the weight map P_{mri} with the source image I_{mri} serving as the guidance image:

$$W_{\text{mri}}^B = \text{GF}_{r1,\epsilon_1}(P_{\text{mri}}, I_{\text{mri}}), \ W_{\text{mri}}^D = \text{GF}_{r2,\epsilon_2}(P_{\text{mri}}, I_{\text{mri}}),$$
$$(8)$$

where $r_1, \epsilon_1, r_2,$ and ϵ_2 the parameters of the guided filter, and W_{mri}^B and W_{mri}^D are the resulting weight maps of the base and detail images. The final results for the MRI are:

$$\bar{B}_{\text{mri}} = W_{\text{mri}}^B \ B_{\text{mri}}, \ \ \bar{D}_{\text{mri}} = W_{\text{mri}}^D \ D_{\text{mri}}. \tag{9}$$

3.4. Weight construction for the US image

The guided filter has shown good results for images corrupted by additive Gaussian noise. However, in practical applications such as US imaging, where the most prominent noise, i.e., speckle, is non-Gaussian, its performance is limited. Recent works on despeckling extended the linear guided filter to a nonlinear filter [10], whose expression can be derived using Bayesian Non-Local Means (NLM). We propose to use the results of [10] to define the US weights.

To illustrate the derivation of the final closed-form weights, a simplified notation will be used by considering an observed speckled image y and a speckle-free image x. The final weights will be subsequently applied to both the base and detail layers $(B_{\text{us}}, D_{\text{us}})$ of the US image. Using these notations, the nonlinear filter is:

$$\hat{x}_i = \sum_j W_{i,j}(y, x^g) \ y_j, \tag{10}$$

where $\hat{x}, y, \ x^g$ are the despeckled image, the speckled observed image, the guidance image, y_j is the jth pixel of y,

and $W_{i,j}(y, x^g)$ is a non-linear weight kernel, where i and j are the pixel positions. We propose to define the guidance image using a simple averaging over every patch in the observed image. In [10], the modified Bayesian NLM is expressed as:

$$\hat{x}_i = \frac{\sum_{j \in \omega_i} p(\mathbf{y}_i|\mathbf{y}_j, \mathbf{x}_i = \mathbf{x}_j, \mathbf{x}^\mathbf{g}) \ p(\mathbf{y}_j, \mathbf{x}_i = \mathbf{x}_j, \mathbf{x}^\mathbf{g}) \ y_j}{\sum_{j \in \omega_i} p(\mathbf{y}_i|\mathbf{y}_j, \mathbf{x}_i = \mathbf{x}_j, \mathbf{x}^\mathbf{g}) \ p(\mathbf{y}_j, \mathbf{x}_i = \mathbf{x}_j, \mathbf{x}^\mathbf{g})},$$

where $\mathbf{y}_i$ and $\mathbf{y}_j$ are the vectorized patches of size $M \times M$ centered at pixels i and j, $\mathbf{x}_i$ and $\mathbf{x}_j$ are the noise-free patches corresponding to the speckled patches $\mathbf{y}_i$ and $\mathbf{y}_j$, and $\mathbf{x}^\mathbf{g}$ is the corresponding patch in the guidance image. For image with fully developed and independent speckle, the conditional probability $p(\mathbf{y}_i|\mathbf{y}_j, \mathbf{x}_i = \mathbf{x}_j, \mathbf{x}^\mathbf{g})$ (denoted as $\pi_{ij}(\boldsymbol{x}, \boldsymbol{y}, \boldsymbol{x}^g)$ for brevity) is:

$$\pi_{ij}(\boldsymbol{x}, \boldsymbol{y}, \boldsymbol{x}^g) = \prod_{m=1}^{M \times M} p(y_{i,m}|y_{j,m}, x_{i,m} = x_{j,m}, x_m^g),$$

where $y_{i,m}, y_{j,m}, x_{i,m}, x_{j,m}$ and x_m^g are associated with the mth pixel in the corresponding patches. Without knowledge of $p(y_{i,m}|y_{j,m})$ and assuming the event $y_{i,m}|y_{j,m}, x_{i,m} = x_{j,m}$ independent on x_m^g, Bayes rule leads to:

$$p(y_{i,m}|y_{j,m}, x_{i,m} = x_{j,m}, x_m^g) \ p(y_{j,m}, x_{i,m} = x_{j,m}, x_m^g)$$
$$\propto \underbrace{p(y_{i,m}, y_{j,m}|x_{i,m} = x_{j,m})}_{\text{likelihood}} \ \underbrace{p(x_{i,m} = x_{j,m}|x_m^g)}_{\text{prior}} \ p(x_m^g),$$

where the likelihood is the data fidelity term, and the prior is related to the probability of having $x_{i,m} = x_{j,m}$ given the corresponding value x_m^g in the guidance image. Due to the high dimensionality of image patches, the prior distribution $p(x_m^g)$ is assumed to be uniform for simplicity. For US images corrupted by a multiplicative speckle noise distributed according to a Rayleigh distribution [4], the following probability density function is obtained:

$$p(y_{i,m}|x_{i,m}) = \frac{y_{i,m}}{x_{i,m}^2 \sigma_\eta^2} \exp\left(\frac{y_{i,m}^2}{x_{i,m}^2 \sigma_\eta^2}\right),$$

for $y_{i,m} > 0$, where σ_η^2 is the noise variance. The conditional density $p(x_{i,m}|x_{i,m}^g)$ is also assumed to be Rayleigh with a parameter $\sigma_g^2(x_{i,m}^g)^2$. The likelihood and prior introduced before can then be computed as follows:

$$p(y_{i,m}, y_{j,m}|x_{i,m} = x_{j,m}) = \int_D p(y_{i,m}|\theta)p(y_{j,m}|\theta)d\theta,$$

$$\propto \frac{y_{i,m}y_{j,m}}{(y_{i,m}^2 + y_{j,m}^2)^{\frac{3}{2}}},$$

$$p(x_{i,m} = x_{j,m}|x_m^g) = \exp\left\{-\text{KL}[p(x_{i,m}|x_{i,m}^g), p(x_{j,m}|x_{j,m}^g)]\right\},$$

$$\propto \exp\left\{-\frac{\left[(x_{i,m}^g)^2 - (x_{j,m}^g)^2\right]^2}{(x_{i,m}^g)^2(x_{j,m}^g)^2}\right\},$$

where D is the domain of pixel values and KL is the symmetric Kullback-Leibler divergence between two Rayleigh distributions (see Appendix A for computation details). The nonlinear weights are finally defined as [11]:

$$W_{i,j}(y,x^g) = \exp\left\{-\frac{1}{K_1}\sum_m \log\left[\frac{(y_{i,m}^2 + y_{j,m}^2)^{\frac{3}{2}}}{y_{i,m}\,y_{j,m}}\right]\right.$$

$$\left.-\frac{1}{K_2}\sum_m \frac{\left[(x_{i,m}^g)^2 - (x_{j,m}^g)^2\right]^2}{(x_{i,m}^g)^2(x_{j,m}^g)^2}\right\}. \quad (11)$$

Using the normalization parameters K_1 and K_2 measuring the relative contributions of y and x^g, one obtains:

$$\bar{x} = \frac{\sum_{j\in\omega_i} W_{i,j}(y,x^g)\,y}{\sum_{j\in\omega_i} W_{i,j}(y,x^g)}. \quad (12)$$

This operation is applied to both base and detail US images.

4. EXPERIMENTS

4.1. Synthetic data from real MR acquisition

To demonstrate the efficiency of the proposed MR/US fusion method, this section first considers a set of synthetic images. The simulations presented hereafter have been obtained using a real high-resolution MR image intentionally degraded to simulate an image closely resembling that obtained for endometriosis diagnosis. The 3D high-resolution MR volume corresponds to an actual pelvic MRI capturing the uterus, bladder, and endometriosis lesions. A blurred and noisy 3D MRI is then generated from this high-resolution MR volume. More precisely, the HR volume was blurred using a 2D Gaussian filter of standard deviation $\sigma^2 = 4$, and then was contaminated by an additive white Gaussian noise (SNR = 18.17 dB), yielding the MR image displayed in Fig. 1(a). A Rayleigh multiplicative noise was applied to the native MR image, yielding the US image in Fig. 1(b) (SNR= 4.8 dB). The size of the average filter was set to 31×31 and the guided filter parameters were fixed to their best values by visual inspection of the fused images, leading to $r_1 = 7$, $\epsilon_1 = 1e^{-4}$, $r_2 = 10$, $\epsilon_2 = 1e^{-6}$. The partial normalization parameters were set to $K_1 = 30$ and $K_2 = 40$ as in [10]. This fixed parameter setting was used for both datasets.
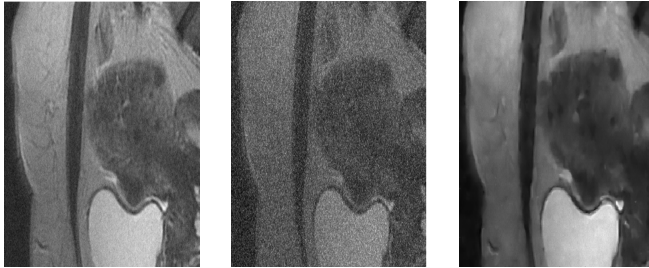
Fig. 1: (a) MR image (b) US image (c) Fused image.

The performance evaluation of the fusion method involved both qualitative analysis through visual inspection of the resultant image and quantitative analysis using the contrast-to-noise ratio (CNR). For two patches extracted from distinct structures, such as the uterus and bladder in this context, CNR is defined as CNR $= \frac{|\mu_i - \mu_j|}{\sqrt{\sigma_i^2 + \sigma_j^2}}$, where $\mu_i, \mu_j, \sigma_i^2, \sigma_j^2$ are the means and standard deviations of two blocks of pixels. The fused image is displayed in Fig. 1(c). This image provides a good compromise between the US and MR data. Specifically, the fused image is less affected by US speckle and MRI blur, provides well-defined contours and good contrast compared to the native MR and US images. The CNR values for the MR and the US images are 35.43 dB and 18.47 dB, whereas the obtained fused image has a CNR equal to 37.54 dB.

4.2. Phantom data

This section evaluates the proposed fusion method on a phantom data. The experimental phantom was designed to replicate the responses of uterine and endometrial tissues to MR and US imaging. It was made of a beef steak on top of which was stuck a polyvinyl alcohol (PVA) phantom, using cyanoacrylate instant glue. On the one hand, the beef meat consists of muscular tissues, exhibiting echogenicity and a response to MR similar to that of uterine tissue. On the other hand, the PVA phantom has roughly the same echogeneicity as the beef meet, but has a different response resulting in high contrast in the MRI. From this viewpoint, its properties are similar to this of endometrium. Finally, the glue between the two structures is visible in US images due to their high resolution but remains absent in MRI due to its limited resolution, simulating the depth of penetration information, a crucial element for the surgery. Additional details about this experiment can be found in [12].
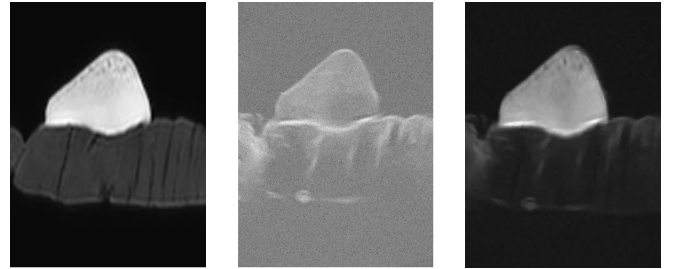
Fig. 2: (a) MR image (b) US image (c) Fused image.

The fused image of Fig. 2(c) has a spatial resolution similar to the US image, and a contrast equivalent to the MRI. In particular, the different structures of interest are much better highlighted: (i) the glue between the steak and the PVA phantom, simulating the depth of penetration, that is indiscernible in MRI due to resolution limitations, is distinctly visible in both the US and fused images; (ii) the contrast between the steak and the PVA is well defined in the MR and fused images, allowing a clear distinction of the parts of interest.

Conventional fusion methods are then compared to the proposed method. Note that contrary to deep learning (DL) meth-
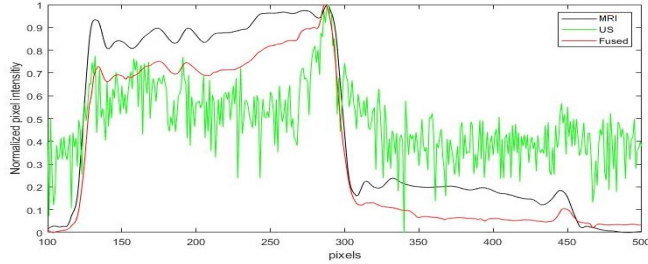
Fig. 3: Normalized pixel intensities of US, MRI, and fused image for a vertical straight line.

ods, which typically require extensive datasets for training, the proposed approach uses only two images (MRI and US) to perform fusion. Acquiring datasets of registered MR and US images for this specific application is challenging due to privacy concerns and the need for patient consent. Given these constraints, opting for DL methods becomes impractical, reinforcing our decision to benchmark against established non-DL fusion techniques. Quantitivative results are provided in Table 1, which compares the CNR values between the PVA phantom and the beef steak for the different images, with fusion models from the literature.

	MRI	US	[4]	[7]	This paper
CNR	54.21	18.91	43.17	44.5	45.17

Table 1: CNR (dB) values for the US, MR and fused images.

While the CNR achieved by the fused image may not match that of the MRI, it represents the optimal compromise between contrast and resolution in our context. The CNR surpasses that of the US, enabling differentiation of various image components. The glue separating the two structures and symbolizing the boundary of the tumor to be incised is more distinctly visible in both the US and fused image compared to the MRI. This improved resolution is visually depicted in Fig. 3, illustrating the differences in pixel intensities.

5. CONCLUSION

This paper introduced a new fusion method for magnetic resonance (MR) and ultrasound (US) images based on guided filtering. The fused image obtained with this method brings together the advantages of both modalities: resolution and contrast. The combination of information arising from both MRI and US into a single image may improve preoperative mapping and surgical plan. An important perspective of this work is to validate the model with other datasets. Future work will be devoted to including the fused image with the video stream collected during laparoscopy, allowing a safer decision-making and therefore a more precise endometriosis surgery.

A. KULLBACK LEIBLER DIVERGENCE BETWEEN TWO RAYLEIGH DISTRIBUTIONS

The Kullback-Leibler divergence between two Rayleigh distributions of densities f_1 and f_2 with parameters σ_1^2 and σ_2^2 denoted as $\mathrm{KLD}(f_1, f_2)$ is defined by:

$$\int_0^\infty \frac{t}{\sigma_1^2} \exp\left(-\frac{t^2}{2\sigma_1^2}\right) \left[\frac{t^2}{2}\left(\frac{1}{\sigma_2^2} - \frac{1}{\sigma_1^2}\right) + \log\left(\frac{\sigma_2^2}{\sigma_1^2}\right)\right] dt,$$

which can be decomposed as the sum of two integrals

$$I_1 = \log\left(\frac{\sigma_2^2}{\sigma_1^2}\right)\int_0^\infty \frac{t}{\sigma_1^2}\exp\left(-\frac{t^2}{2\sigma_1^2}\right)dt = \log\left(\frac{\sigma_2^2}{\sigma_1^2}\right),$$

and

$$I_2 = \frac{1}{2}\left(\frac{1}{\sigma_2^2} - \frac{1}{\sigma_1^2}\right)\int_0^\infty \frac{t^3}{\sigma_1^2}\exp(-\frac{t^2}{2\sigma_1^2})dt = \frac{\sigma_1^2}{\sigma_2^2} - 1.$$

The symmetric Kullback-Leibler divergence between the densities f_1 and f_2 is:

$$\mathrm{KL}(f_1, f_2) = \mathrm{KLD}(f_1, f_2) + \mathrm{KLD}(f_2, f_1) = \frac{(\sigma_1^2 - \sigma_2^2)^2}{\sigma_1^2 \sigma_2^2}.$$

B. REFERENCES

[1] U. Pietrzyk, K. Herholz, A. Schuster, H.-M. Stockhausen, H. Lucht, and W.-D. Heiss, "Clinical applications of registration and fusion of multimodality brain images from PET, SPECT, CT, and MRI," *European journal of radiology*, vol. 21, no. 3, pp. 174–182, 1996.

[2] A. Wong and W. Bishop, "Efficient least squares fusion of MRI and CT images using a phase congruency model," *Pattern Recognition Letters*, vol. 29, no. 3, pp. 173–180, 2008.

[3] W. Vogel V, W. Oyen, J. Barentsz, J. Kaanders, and F. Corstens, "PET/CT: panacea, redundancy, or something in between?," *Journal of Nuclear Medicine*, vol. 45, no. 1, pp. 15S, 2004.

[4] O. El Mansouri, F. Vidal, A. Basarab, P. Payoux, D. Kouamé, and J.-Y. Tourneret, "Fusion of Magnetic Resonance and Ultrasound images for endometriosis detection," *IEEE Trans. Image Process.*, vol. 29, pp. 5324–5335, 2020.

[5] Y. El Bennioui, A. Bruguier, F. Vidal, A. Basarab, and J.-Y. Tourneret, "Fusion of Ultrasound and Magnetic resonance images for endometriosis diagnosis: A non-parametric approach," in *Proc. Workshop on Computational Advances in Multi-Sensor Adaptive Processing (CAMSAP)*, San José, Costa Rica, Dec. 2023.

[6] K. He, J. Sun, and X. Tang, "Guided image filtering," *IEEE Transactions on Pattern Analysis and Machine Intelligence*, vol. 35, no. 6, pp. 1397–1409, 2013.

[7] S. Li, X. Kang, and J. Hu, "Image fusion with guided filtering," *IEEE Transactions on Image Processing*, vol. 22, no. 7, pp. 2864–2875, 2013.

[8] Y. El Bennioui, F. Vidal, A. Basarab, and J.-Y. Tourneret, "Joint registration and fusion of 3D Magnetic resonance and 2D ultrasound images using endometriosis surgery," in *Proc. European Signal Processing Conference (EUSIPCO)*, Helsinki, Finland, Sep. 2023.

[9] R. C. Gonzalez and R. E. Woods, *Digital image processing*, Prentice Hall, Upper Saddle River, N.J., 2008.

[10] W. Ni and X. Gao, "Despeckling of SAR image using generalized guided filter with Bayesian nonlocal means," *IEEE Transactions on Geoscience and Remote Sensing*, vol. 54, no. 1, pp. 567–579, 2016.

[11] C.-A. Deledalle, L. Denis, and F. Tupin, "Iterative weighted maximum likelihood denoising with probabilistic patch-based weights," *IEEE Trans. Image Process.*, vol. 18, no. 12, pp. 2661–2672, 2009.

[12] F. Vidal, O. El Mansouri, D. Kouamé, and A. Basarab, "On the design of a pelvic phantom for Magnetic Resonance and Ultrasound image fusion," in *Proc. IEEE IUS Symp.*, Glasgow, UK, 2019, pp. 2400–2403.